nature communications

Article

https://doi.org/10.1038/s41467-024-54660-w

Superconductivity in an infinite-layer nickelate superlattice

Received: 2 August 2024

Accepted: 14 November 2024

Published online: 25 November 2024

Check for updates

Wen Xiao[1], Zhan Yang[1,2], Shilin Hu[1], Yuzhou He[3], Xiaofei Gao[1], Junhua Liu[1], Zhixiong Deng[1], Yuhao Hong[1], Long Wei[1], Lei Wang[1], Ziyue Shen[1], Tianyang Wang[1], Lin Li[1], Yulin Gan[1] ✉, Kai Chen[1] ✉, Qinghua Zhang[3] ✉ & Zhaoliang Liao[1] ✉

Recent observations of superconductivity in infinite-layer nickelates offer insights into high-temperature superconductivity mechanisms. However, defects and dislocations in doped films complicate the realization of superconductivity, limiting current research to superconducting nickelate heterostructures. The lack of research on superconductivity in superlattices composed of ultrathin nickelates severely impedes not only the exploration of the interface effect on superconductivity, but also the utilization of heterostructure engineering for exploring higher superconducting temperature T_c. Here, we demonstrated superconducting infinite-layer nickelate superlattices $[(Nd_{0.8}Sr_{0.2}NiO_2)_8/(SrTiO_3)_2]_{10}$ via topotactic reduction. Our study uncovered that only above a critical thickness can high-quality superlattices be achieved, with structural formation dependent on nickelate layer thickness. The superconducting superlattice showed a T_c of 12.5 K and a 2D superconducting feature, indirectly indicate the intrinsic superconductivity of infinite-layer nickelates. Our study offers promising avenues for delving into the superconducting mechanism and for exploring multilevel interface engineering of infinite-layer nickelates, thus opening new horizons for the study of infinite-layer nickelates.

Since the discovery of high-temperature superconductivity (HTSC) in copper oxides in 1986[1], there has been an increasing interest in searching for similar unconventional HTSC in other systems. In 2019, Li et al. firstly realized 9–15 K superconductivity in the infinite-layer $Nd_{0.8}Sr_{0.2}NiO_2$ thin films by soft-chemistry topotactic reduction[2]. Subsequently, some extended rare-earth nickelate superconducting films were discovered[3–7]. The recent discovery of superconductivity in pressure-induced $La_3Ni_2O_7$[8] and $La_4Ni_3O_{10}$[9] single crystals has positioned nickelates as a novel addition to the HTSC family. Infinite-layer nickelates and cuprates share many similarities, such as two-dimensional infinite-layer structure, superconducting dome determined by doping level[3,4,10,11], d-wave systems[12,13], and band dispersion[14,15], etc. However, nickelates show some intrinsic differences. For parent compounds, nickelates are closer to Mott-Hubbard feature, while cuprates are in the charge-transfer regime of the Zaanen–Sawatzky–Allen scheme[16,17]. The nickelate parent compounds exhibit a metallic ground state[2], contrasting the mott insulating state of cuperates[18]. Other features, including the absence of long-range antiferromagnetic orders[19,20] and multiorbital physics[21–23] are also different from that in cuprates. Nevertheless, employing comparable methods utilized in the study of cuprates to investigate the underlying mechanism of superconductivity in infinite layers of nickelates can still be a valuable approach.

Interface engineering serves as a potent method for modulating the nature of superconductivity. Induced or enhanced superconductivity

[1]National Synchrotron Radiation Laboratory, School of Nuclear Science and Technology, University of Science and Technology of China, Hefei, China. [2]School of Physics, Zhengzhou University, Zhengzhou, China. [3]Beijing National Laboratory for Condensed Matter Physics, Institute of Physics, Chinese Academy of Sciences, Beijing, China. ✉e-mail: ylgan@ustc.edu.cn; kaichen2021@ustc.edu.cn; zqh@iphy.ac.cn; zliao@ustc.edu.cn

has been observed at various interfaces, including $LaAlO_3/SrTiO_3$ 2DEGs[24], $La_{1.55}Sr_{0.45}CuO_4/La_2CuO_4$[25], FeSe/$SrTiO_3$[26] and $CaCuO_2/SrCuO_2$ superlattices[27]. Therefore, it promotes the puzzles whether interfaces play a role in influencing the superconductivity in infinite-layer nickelates. However, superconductivity in infinite-layer nickelates can currently only be achieved in a single film of finite thickness. Some efforts had been made in infinite-layer $LaNiO_{2+x}/LaGaO_3$[28] and $NdNiO_2/SrTiO_3$[29] superlattices but no superconducting feature was found. One contributing factor could be the formation of a mixed Ruddlesden–Popper (RP) secondary phase during the growth process[30]. Additionally, the de-embedding of oxygen[31] and the presence of hydrogen[32] during the reduction process also affect superconductivity. Furthermore, significant interfacial polarization and surface reconstruction occur at the interface between the polar infinite-layer nickelates and the non-polar oxides[29,33,34]. All of these issues make the realization of high-quality superconducting infinite-layer nickelate superlattices and the interface modulation very challenging. Nevertheless, the achievement of superlattice superconductivity and the exploration of its distinctions from single thin films remain crucial for advancing our understanding of the mechanisms underlying interfacial interactions in the superconductivity of infinite-layer nickelates thin films.

Here, we demonstrated the realization of superconductivity in $(Nd_{0.8}Sr_{0.2}NiO_2)_n/(SrTiO_3)_m$ superlattices. By reducing the pristine $(Nd_{0.8}Sr_{0.2}NiO_3)_n/(SrTiO_3)_m$ superlattices which were grown by pulsed laser deposition with CaH_2, we found that the as-reduced films exhibit structure changes which are dependent on the thickness of nickelate layers. In $(Nd_{0.8}Sr_{0.2}NiO_2)_3/(SrTiO_3)_2$ superlattice with a thickness below a critical value of 5 u.c., mixed phases were observed, while the 8 u.c. nickelates in $(Nd_{0.8}Sr_{0.2}NiO_2)_8/(SrTiO_3)_2$ superlattice exhibit a well-defined infinite-layer structure. Only the superlattices with infinite-layer nickelates exhibit superconductivity with an onset transition temperature T_c of 12.5 K, whereas the mixed phase superlattices show insulating behaviors. Detailed experimental investigations of transport properties show that the superconducting superlattice displays a 2D superconducting feature with anisotropic cahracteristic[35–39]. The consistent characterization with a single film suggests that the interface has little effect on its superconducting properties, indirectly demonstrating that the superconductivity of infinite-layer nickelate is intrinsic.

Results

Thickness driven structure change in superlattices

Nickelate superlattices (SL) $[(Nd_{0.8}Sr_{0.2}NiO_3)_n/(SrTiO_3)_2]_{10}$ (referred as N_n/S_2) were initially deposited on $SrTiO_3$ substrates by pulsed laser deposition (PLD) and subsequently fully reduced using CaH_2, as detailed in the methods section. The as-reduced SLs are denoted as R-N_n/S_2. The thicknesses of the pristine and as-reduced SLs thicknesses are controlled by the in-situ reflection high-energy electron diffraction and further confirmed by fitting X-ray reflectivity (XRR) (Fig. 1b and Supplementary Fig. S8c). The crystal structures were characterized by X-ray diffraction (XRD) θ–2θ symmetric scans, as depicted in Fig. 1a. The as-grown N_3/S_2 (black) and N_8/S_2 (blue) SLs exhibit distinct superlattice features with satellite peaks, indicating the absence of secondary phase. Reciprocal space mapping (RSM) corresponding to $SrTiO_3$ (103) reflections in Fig. 1c and Supplementary Fig. S8a confirm coherent strain of the SLs on the $SrTiO_3$ substrates. Even after an extended reduction process, the XRD patterns retain clear SL main peaks and satellite peaks. The RSMs in Fig. 1d and Supplementary Fig. S8b demonstrate that the as-reduced SLs still remain fully strained to $SrTiO_3$ substrates.

Compared to the pristine SLs, the peaks of R-N_8/S_2 (green) exhibit a rightward shift towards higher values, indicating the formation of

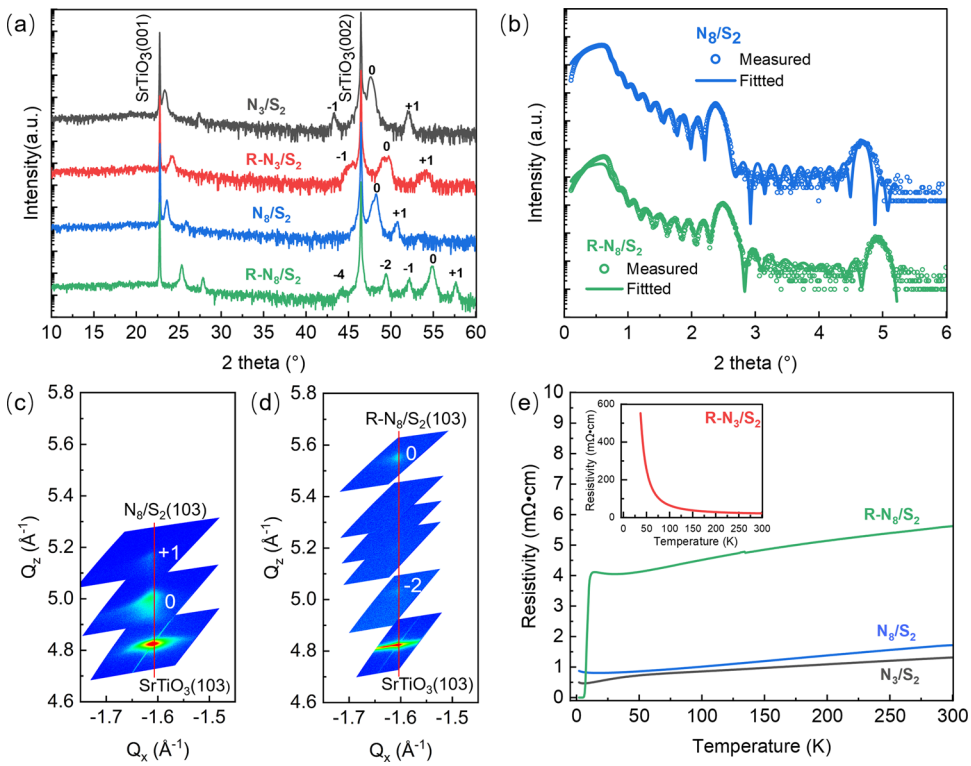

Fig. 1 | Structure and electrical transport of as-grown $[(Nd_{0.8}Sr_{0.2}NiO_3)_m/(SrTiO_3)_2]_{10}$ (N_m/S_2) and reduced $[(Nd_{0.8}Sr_{0.2}NiO_2)_m/(SrTiO_3)_2]_{10}$ (R- N_m/S_2) nickelate superlattice(SL) films. a θ-2θ XRD spectra of as-grown N_3/S_2 (black), N_8/S_2 (blue) and reduced R-N_3/S_2 (red), R-N_3/S_2 (green). Main and satellite peaks of SLs are numerically identified. **b** Measured X-ray reflectivity (XRR) and fitted of N_8/S_2 and R-N_8/S_2 SLs marked with hollow points and solid lines, respectively. **c** and **d** show reciprocal space mapping(RSM) of N_8/S_2 and R-N_8/S_2 (103) peaks. The main and satellite peaks corresponding to the XRD pattern are also numerically marked. **e** Temperature dependence of the resistivity ρ(T) of SLs.

infinite-layer $Nd_{0.8}Sr_{0.2}NiO_2$[2]. The out-of-plane lattice constant c(R-N_8/S_2) is extracted to be 3.34 Å according to the main peak position. In contrast, the rightward shift value for R-N_3/S_2 (red) is much smaller than that of R-N_8/S_2, with a peak position of 49.75°, corresponding to c(R-N_3/S_2) = 3.66 Å. This observation is reminiscent of findings in $SrCuO_2$ SLs, where discrepancies between plane-type and chain-type crystal structures were noted[40,41]. However, the chain-type $LaNiO_2$ shows a larger c-axis constant than the $SrTiO_3$ substrate[42], contrary to our XRD data, suggesting that the chain-type structure does not account for the difference in lattice constants. Nevertheless, the presence of the $SrTiO_3$ layer in the N_3/S_2 SL significantly hinders the reduction condition of the embedded $Nd_{0.8}Sr_{0.2}NiO_2$ layers, which was not observed in N_8/S_2 SL. Therefore, question will arise that is there a critical thickness in $Nd_{0.8}Sr_{0.2}NiO_2$ SL for the structure change, similar to that occurring in $SrCuO_2$ SL[41,43] ? Our preliminary data indeed indicates evidence of nickelate thickness-driven structural changes and the existence of a critical thickness of approximately ~5 u.c. (see Supporting Information, Supplementary Fig. S3). Below and above 5 u.c., the superlattice exhibit significantly different lattice constants. What is more, the change in lattice structure is not attributed to inadequate reduction processes (see the detailed discussion in the Supporting Information).

Figure 1e shows the temperature-dependent resistivity of pristine N_3/S_2, N_8/S_2 and as-reduced R-N_3/S_2, R-N_8/S_2. Both the as-grown N_3/S_2 and N_8/S_2 exhibit metallic behavior, consistent with previous report[2]. After reduction, R-N_8/S_2 displays metallic temperature dependence above 40 K and transitions to a superconducting state with an onset temperature of 12.5 K ($T_{c,onset}$), reaching zero resistance at 5.5 K ($T_{c,0}$). This transition temperature aligns with previous observations in 10 nm $Nd_{0.8}Sr_{0.2}NiO_2$/$SrTiO_3$ single films[2]. It is noteworthy that our superlattice allows a thinner thickness of the nickelate while still maintaining a high T_c value, whereas for thinner single films, the T_c value decreases monotonically with thickness (for a single $Nd_{0.8}Sr_{0.2}NiO_2$/$SrTiO_3$ film of 4.6 nm, i.e., ~14 uc, the $T_{c,onset}$ is only ~6.5 K)[44]. Conversely, R-N_3/S_2 demonstrates insulating transport behavior across the entire temperature range from 30 to 300 K (refer to the inset in Fig. 1b). Below 30 K, the resistance measurement falls outside of our electronic measurement range.

The structural differences between the two superlattices were further investigated using scanning transmission electron microscopy (STEM) techniques. Figures 2a and 2e schematically shows the superlattice stacking sequence. For R-N_3/S_2, the first layer is of 4 u.c. $Nd_{0.8}Sr_{0.2}NiO_2$, which was used to reflect the evolution for structure change. The high annular angle dark field (HAADF) STEM images for large region of R-N_3/S_2 and R-N_8/S_2 are shown in Supplementary Fig. S9, which reveal very sharp interfaces between $Nd_{0.8}Sr_{0.2}NiO_2$ and $SrTiO_3$ in the as-reduced superlattices. In both R-N_3/S_2 and R-N_8/S_2, only very few RP defects were observed, demonstrating the stabilizing effect of $SrTiO_3$ interfacial layer on nickelate monostructures, which may be the reason that our superlattices have higher T_c values

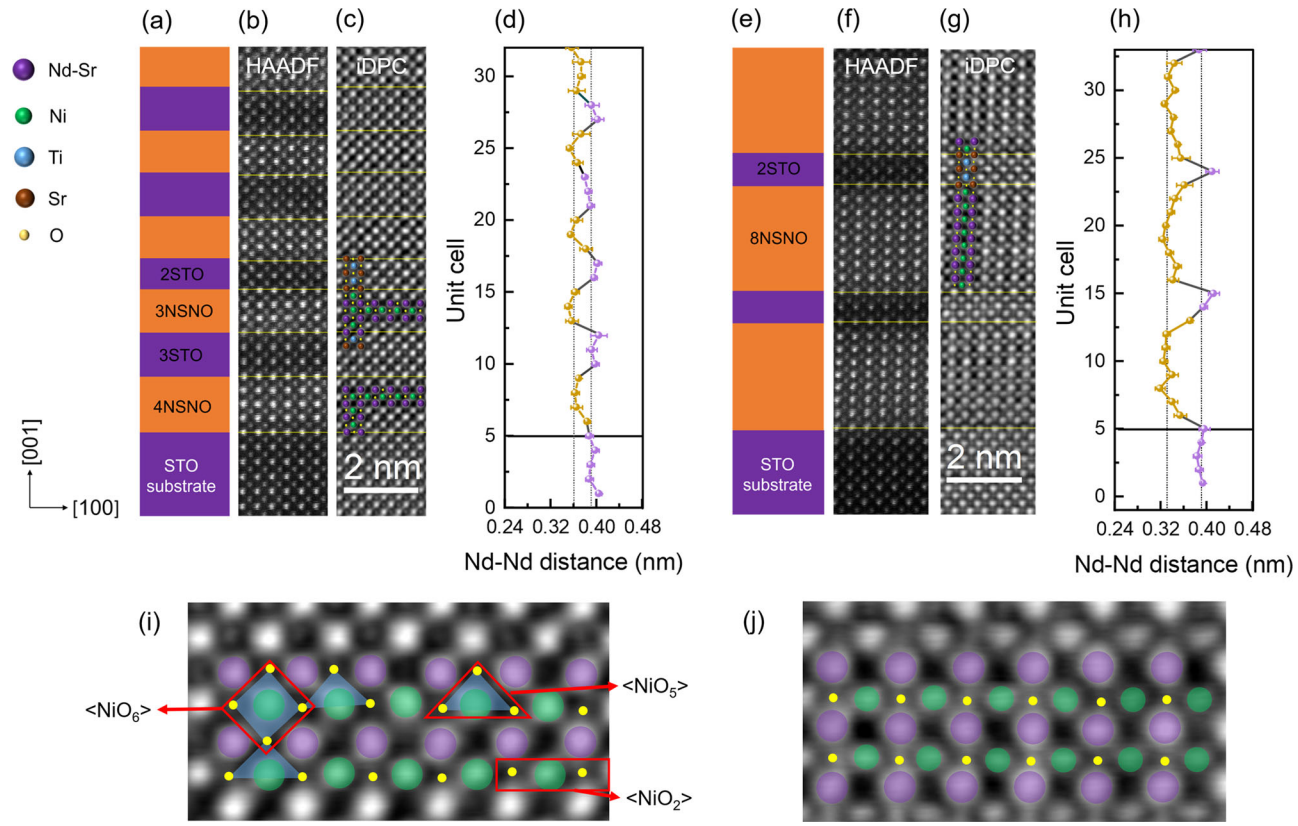

Fig. 2 | High-resolution STEM images of reduced superlattices (R-N_m/S_2). **a** Schematic structure of the R-N_3/S_2 superlattice, the nickelate (NSNO) and strontium titanate (STO) layers in the superlattice are distinguished by orange and purple colors, respectively. **b** Atomically resolved HAADF-STEM image of R-N_3/S_2. **c** iDPC-STEM image of R-N_3/S_2. Different colored balls represent different atoms: Nd-Sr (purple), Ni (green), Ti (blue), Sr (brown), O (yellow). **d** Variation of the A-A out-of-plane distance with the number of unit cells counted from HAADF image, the colors corresponding to **a** are used to display the out of plane distance of various layers. **e** Schematic structure of the R-N_8/S_2 superlattice. **f** Atomically resolved HAADF-STEM image of R-N_8/S_2. **g** iDPC-STEM image of R-N_3/S_2. **h** Variation of the Nd-Nd out-of-plane distance with the number of unit cells counted from HAADF image. **i** Zoom-in iDPC-STEM image of nickelate layers in R-N_3/S_2. Nickelate units with different levels of reduction are indicated by shadows defined by red boxes, from left to right, rhombus (<NiO_6> octahedron), triangles (<NiO_5> pentahedron) and rectangles (<NiO_2> infinite-layer). **j** Zoom-in iDPC-STEM image of nickelate layers in R-N_8/S_2. The error bars in **d** and **h** are calculated by averaging seven unit cells on each row.

compared to single films of similar thicknesses. The atomic structures of the as-reduced films are shown by zoom in HAADF-STEM images (see Fig. 2b, f). For the bright field image, the bright intensity of spots in an atomically resolved image is positively correlated with the square of its atomic number Z ($I \propto Z^2$). In this way, light and heavy atoms can be clearly distinguished according to their image contrast. It can be seen that the $Nd_{0.8}Sr_{0.2}NiO_2$ and $SrTiO_3$ layers grow epitaxially with respect to each other along the [001] growth direction.

For as-reduced nickelate layers, oxygen de-embedding is a noteworthy issue. The iDPC-STEM is an effective method to avoid electron damage while preserving the lining of both light and heavy atoms, and has greater advantages over the HAADF-STEM technique in studying the distribution and defects of oxygen atoms[45]. Atomically resolved iDPC-STEM images corresponding to the HAADF-STEM images are shown in Fig. 2c, g. The oxygen atoms in <TiO_6> octahedron of $SrTiO_3$ and qusi−2D infinite-layer NiO_2 plane of $Nd_{0.8}Sr_{0.2}NiO_2$ are clearly identified. Local atomic distributions are highlighted with different colored spheres. In the case of R-N_8/S_2 shown in Fig. 2g, j, it is evident that the infinite-layer $Nd_{0.8}Sr_{0.2}NiO_2$ alternates with the perovskite $SrTiO_3$, and a collapse of the $Nd_{0.8}Sr_{0.2}NiO_2$ unit cell along the c-axis direction is observable. This observation suggests that the nickelate layers, when capped by the $SrTiO_3$ intermediate layer, are more prone to lose apical oxygen atoms during hydrogenation-chemical reduction, leading to the collapses into an infinite-layer structure, as previously reported[2,46]. Instead, only partial apical oxygen atoms are de-embedding in R-N_3/N_2 (Fig. 2c, i), resulting in a disordered mixture of planar-type infinite-layer, pyramidal and octahedron structures. Such disordering structure is also observed in 4 u.c. $Nd_{0.8}Sr_{0.2}NiO_2$ layer which was deliberately inserted first into N_3/N_2 SL to obtain more thickness effect microstructure. It can be concluded that STEM also revealed same critical thickness for structure change from disordering structure to ordering infinite layer structure. This disorder increases as the nickelate layer approaches the $SrTiO_3$ interlayer at interface, where removing apical oxygen becomes more difficult. Such disordered distribution and inhomogeneous structure may be responsible for its transformation into an insulator, which was also observed in partially reduced $Pr_{0.8}Sr_{0.2}NiO_{2+x}$[34]. In addition, Nd-O layers are observed at the $Nd_{0.8}Sr_{0.2}NiO_2$/$SrTiO_3$ interface in both two SLs, serving to alleviate the strong charge field induced by the polar interface[33].

Figures 2d and 2h illustrates the profiles of Nd-Nd out-of-plane distance across R-N_3/S_2 and R-N_8/S_2 superlattices derived from HAADF images. The data are averaged over seven vertical profiles. The Nd-Nd out-of-plane distance represents the lattice constant of the *c*-axis per unit cell. It can be seen that the *c*-axis lattice parameters of the $SrTiO_3$ interlayers in both two SLs are distributed around 0.39 nm, which is consistent with the $SrTiO_3$ substrate. The uniform in-plane dimensions indicate that the $SrTiO_3$ interlayers maintain a cubic perovskite structure, unaffected by prolonged topotactic reduction. For the nickelates layers, the *c*-axis lattice constants of R-N_3/S_2 fluctuate around 0.36 nm, whereas it is 0.33 nm in R-N_8/S_2, aligning with the values obtained from XRD patterns. The characterizations of crystal structure based on the XRD and STEM reveal that the presence of residual apical oxygen directly hinders the reduction of the out-of-plane lattice constant of nickelate layers. Furthermore, local lattice extensions of 0.4 nm are observed at the $SrTiO_3$ layer interfaces, which is attributed to the mixing stoichiometry of Ti and Ni in the interface layer[33].

Large orbital polarizations are frequently observed in complex oxides with quasi−2D structures, including high-T_c cuprates like $YBa_2Cu_3O_7$[47], $SrCuO_2$ heterostructures[40,41] and nickelates featuring infinite-layer configurations[17,28,48]. Such orbital polarization can be explored by measurement of linearly polarized X-ray absorption spectroscopy. In Fig. 3a, the schematic diagram illustrates the X-ray linear dichroism (XLD) measurement using two light polarizations. The intensity with electric vector E along the in-plane polarization (E//ab) corresponds to the occupation of $d_{x^2-y^2}$ orbitals, while the out-of-plane polarization (E//c) reflects the occupation of $d_{3z^2-r^2}$ orbitals. As shown in Fig. 3b, we compare the polarization dependence of the XAS spectra at the Ni $L_{2,3}$-edge. Firstly, XAS for R-N_3/S_2 and R-N_8/S_2 both show a main absorption peak closely resembling Ni^{1+} in $NdNiO_2$[17]. The Ni L_3-edge of R-N_3/S_2 shows a higher peak energy (~0.2 eV) than R-N_8/S_2, suggesting a higher Ni valence state in R-N_3/S_2, corresponding to the fewer oxygen vacancies in R-N_3/S_2. Moreover, significant differences are observed in the XAS spectra along different polarizations in both SLs, highlighting the preferred orbital occupation in both infinite-layers. The XLD intensity (defined by $I_{E//ab}$ - $I_{E//c}$) shown in Fig. 3c reveals strong positive dichroism in both SLs, which can be attributed to the unoccupied $d_{x^2-y^2}$ orbital in the low spin state picture[48]. It indicates that the orbitals along *z*-axis are more occupied in both mixed-structure R-N_3/S_2 and infinite-layer R-N_8/S_2. This phenomenon is attributed to the lower Ni-O bonding energy of apical oxygen in <NiO_6> octahedra[42], facilitating square-planar coordination of Ni atoms after topochemical reduction. On this basis, the crystal field splitting in the e_g orbitals is greatly enhanced, leading to the lower energy levels and higher electron occupancy in the $d_{3z^2-r^2}$ orbitals compared to the $d_{x^2-y^2}$ orbitals, thereby inducing significant orbital polarization. Notably, unlike the findings in $SrCuO_2$ superlattices[40,41], no significant thickness-dependent XLD intensity differences were observed in the infinite-layer nickelate superlattices. This observation further supports the absence of chain-like structures in R-N_3/S_2, as evidenced by STEM images and XRD patterns.

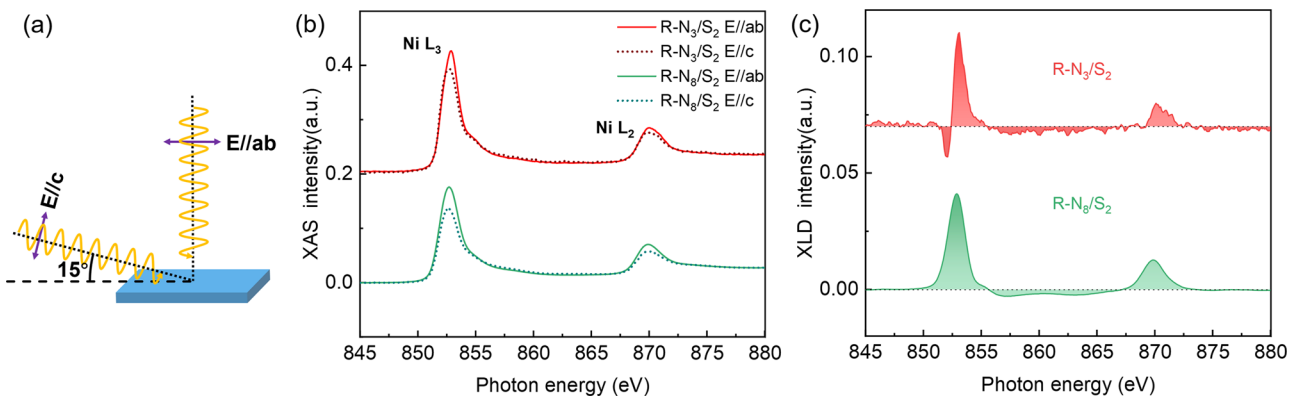

Fig. 3 | X-ray linear dichroism. a Schematic diagram of X-ray linear dichroism(XLD) measurement, the grazing incidence angle is 15°. **b** Polarization dependent X-ray absorption spectra of Ni $L_{2,3}$ edges in reduced R-N_3/S_2 (red) and R-N_8/S_2 (green). The vertical incidence of linearly polarized light onto the sample surface are depicted by solid lines, whereas the grazing incidence of linearly polarized light are illustrated by dashed lines. **c** The X-ray linear dichroism(XLD) defined by $I_{XLD} = I_{E//ab} - I_{E//c}$, indicated by shaded area.

https://doi.org/10.1038/s41467-024-54660-w

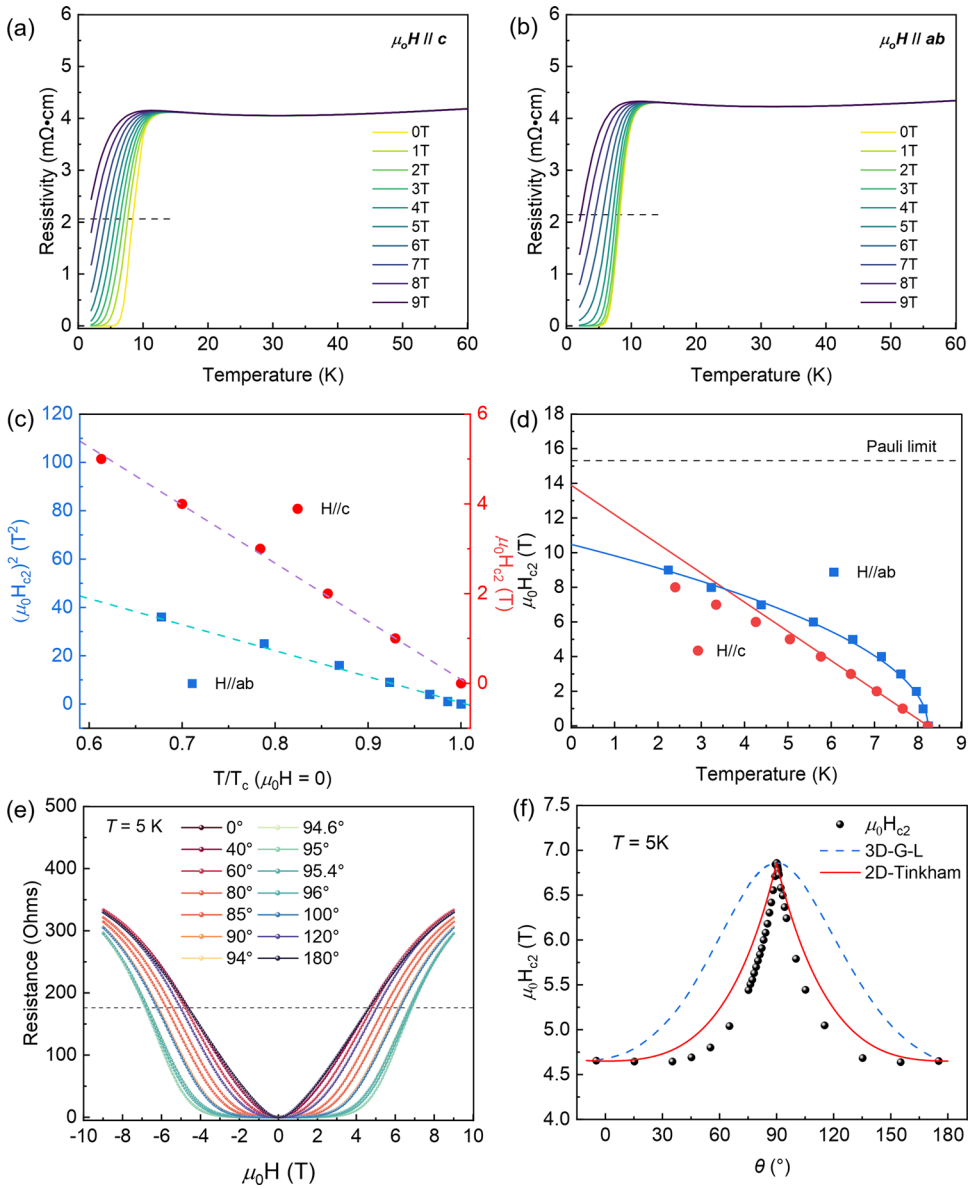

Fig. 4 | Magnetic transport properties and the upper critical fields (H_{c2}) anisotropy of superconducting R-N_8/S_2 superlattice film. Temperature dependence of the resistivity under different magnetic fields from 0 to 9 T (**a**) along *c*-axis and (**b**) in the *a*-*b* plane below 60 K. **c** Temperature dependence of $(H_c)^2$ (μ_0H || *ab*) and H_c (μ_0H || *c*) near T_c. The purple and blue dashed lines are the corresponding linear fits. **d** Temperature dependence of the upper critical fields for both directions. The solid line is the data fitted around the T_c using the (modified) GL theory, and the dashed lines indicate the Pauli limit of $H_{Pauli} = 1.86\ T_{c0}$. **e** Magnetic field dependence of the resistance measured with different magnetic field orientations at 5 K, and the top right inset shows a configuration for measurements. **f** Polar angular dependence of the critical magnetic field $H_{c2}(\theta)$ at T = 5 K. The red solid line and the blue dotted line are the fittings with the 2D-Thikham model and the 3D anisotropic G-L model. All the H_{c2} data are extracted at 50% of the normal state resistance or resistivity.

Superconducting properties of $[(Nd_{0.8}Sr_{0.2}NiO_2)_8/(SrTiO_3)_2]_{10}$ superlattice

The superconducting properties of R-N_8/S_2 were further investigated by measuring the magnetoresistance. Figures 4a and 4b display the temperature-dependent magnetoresistance (MR) under the out-of-plane (μ_0H_c//c) and in-plane (μ_0H_c//ab) magnetic fields ranging from 0 to 9 T. Little magnetoresistance is observed in the normal state, whereas the superconducting state at lower temperature is significantly suppressed by the magnetic field. Moreover, the effect of magnetic field orientations on superconducting suppression varies considerably. The ρ(T) curves reveal a denser behavior when the magnetic field is applied transversely. Similar distinctions are observed in the magnetic-field-dependent MR shown in Supplementary Fig. S11a, S11b. These observations indicate the anisotropy in the superconductivity of the R-N_8/S_2 superlattice.

To further comprehend the superconductivity anisotropy in R-N_8/S_2, we extracted the variation of the upper critical field H_{c2} with $T_{c,mid}$, where the resistivity reaches 50% of the normal state (Fig. 4d). Figure 4c illustrates the critical field in both directions versus the temperature point near $T_{c,0}$ ($\mu_0H_c = 0$). For μ_0H_c//c, the upper critical field follows a linear relationship with temperature near $T_{c,0}$, while a $(T_c\text{-}T)^{1/2}$-dependence is followed for μ_0H_c//ab. This is commonly observed in two-dimensional superconductors[49–51]. It implies the possible 2D superconducting characteristic of R-N_8/S_2, which is consistent with the square-planar NiO_2 plane geometry. This behavior can be well

described by the 2D Ginzburg-Landau (G-L) formula[52] as

$$H_{c2,\perp}(T) = \frac{\Phi_0}{2\pi\xi_{ab}^2(0)}\left(1-\frac{T}{T_c}\right) \quad (1)$$

$$H_{c2,||}(T) = \frac{\sqrt{12}\Phi_0}{2\pi\xi_{ab}(0)d_{sc}}\left(1-\frac{T}{T_c}\right)^{\frac{1}{2}} \quad (2)$$

where Φ_0 is the flux quantum, $\xi_{ab}(0)$ is the in-plane G-L coherence length in the zero-temperature and d_{sc} is the superconducting thickness. Using the above equations to fit the data, we derived $\xi_{ab}(0) = 48.7$ Å, and $d_{sc} = 223.5$ Å, which are consistent with previous reports on $Nd_{0.775}Sr_{0.225}NiO_2$ films[35]. Furthermore, both the in-plane and the out-of-plane upper critical fields remain below the Bardeen–Cooper–Schrieffer Pauli limit, as shown by the fitted curves (H_{Pauli}, $\mu = 1\,\mu B = 1.86 \times T_{c,0}$).

To confirm the two-dimensional superconducting feature of R-N_8/S_2, we measured the angular dependence of H_{c2} of R-N_8/S_2 at 5 K. Figure 4e shows the MR curves at different θ values, and the inset shows a configuration for measurements. By extracting the values of the critical field at different angles, the angular-dependent $H_{c2}(\theta)$ curves can be obtained, as shown in Fig. 4f. A clear cusp-like peak can be observed when θ approach 90° (μ_0H//ab), which can be described by the 2D-Tinkham formula for 2D superconductors (red solid line)[50], which is expressed as

$$\left(\frac{H_{c2}(\theta)\sin\theta}{H_{c2}^{||}}\right)^2 + \left|\frac{H_{c2}(\theta)\cos\theta}{H_{c2}^{\perp}}\right| = 1 \quad (3)$$

In contrast, the peak cannot be reproduced by 3D anisotropic G-L model (blue dotted line), which is expressed as

$$H_{c2}(\theta) = \frac{H_{c2}^{||}}{\left(\sin^2\theta + \gamma^2\cos^2\theta\right)^{\frac{1}{2}}} \quad (4)$$

where anisotropy ratio $\gamma = H_{c2}^{||}/H_{c2}^{\perp}$. These results qualitatively indicate the 2D feature of R-N_8/S_2. However, unlike the large γ of conventional 2D superconductors[50], the γ of R-N_8/S_2 approaches 1 at low temperature. This behavior may represent a unique characteristic of nickelate thin-film superconductors, which was also found in $Nd_{0.8}Sr_{0.2}NiO_2/SrTiO_3$ single films with 2D superconducting feature[38,53].

Figure 5a presents the current-voltage (I-V) characteristics at different temperatures. A zero-voltage flat state in the I-V characteristic curves is observed at low temperatures, which indicates the presence of a superconducting state. As temperature increases towards the normal state, the plateau disappears and is changed to a linear characteristic. For superconducting states, the increasing bias current would induce a superconducting transition at a critical value, i.e., the critical current value I_c. The evolution of I_c values from 2 K-5 K summarized in Fig. 5b shows robust current tolerance at the milliamp level in R-N_8/S_2. Furthermore, the Berezinskii-Kosterlitz-Thouless (BKT) transition was studied in R-N_8/S_2. This transition is a notable feature in 2D superconductors, indicating a shift from unpaired vortices and antivortices to bound vortex–antivortex pairs[54]. The BKT transition appears as a power-law exponential jump at the zero-current limit of the current-voltage characteristic curves, with the BKT temperature (T_{BKT}) typically defined as the temperature where $V \propto I^3$. Figure 5c illustrates the I-V characteristic curves in the second quadrant near the critical current on a logarithmic scale. As the temperature changes

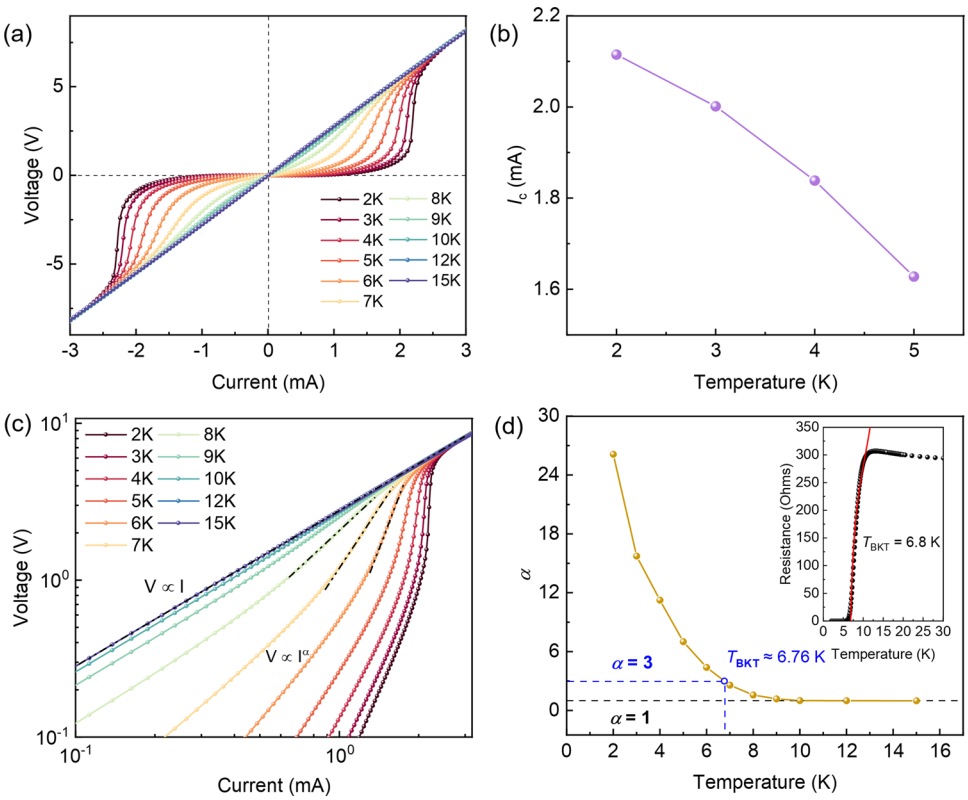

Fig. 5 | Critical current and the BKT transition temperature of R-N_8/S_2. a I-V curves at different temperatures. **b** Dependence of critical current with temperature. **c** Plots of the I-V curves at different temperatures on a log-scale. The relationship between current and voltage can be represented by the slope of the fitted dotted line. **d** Temperature dependence of α in $V \propto I^{\alpha}$. T_{BKT} of R-N_8/S_2 are indicated by the blue hollow dot. The inset shows the resistance transition at zero magnetic field, and the red solid line represents the BKT transition using the Halperin-Nelson equation.

from normal to the superconducting states, the I-V characteristic changes from linear (V∝I) to exponential (V∝I$^{\alpha}$) dependence, demonstrating the typical 2D superconductor BKT transition feature of R-N_8/S_2. We further extracted the power index values α as a function of temperature from slopes in the log-log scale I-V characteristic curves at different temperatures (Fig. 5d), yielding an extrapolated T_{BKT} of ~6.76 K. In addition, the R(T) curve can be reproduced by BKT transition using Halperin-Nelson equation[55] (red solid curve in the inset of Fig. 5d), $R = R_0 \exp\left[-2b\left(\frac{T_{c0}-T}{T-T_{BKT}}\right)^{\frac{1}{2}}\right]$, where R_0 and b are material parameters. The fitting results give a BKT transition temperature of T_{BKT} = 6.80 K, which is consistent with the data extrapolated from the I-V curves.

Discussion

Overall, the R-N_8/S_2 superlattice exhibits superconductivity with an onset transition temperature of 12.5 K, which is consistent with the T_c range of 9–15 K in 10-nm-thick $Nd_{0.8}Sr_{0.2}NiO_2$ films grown on $SrTiO_3$ substrates[2]. Different magnetoresistive responses to magnetic fields along in-plane and out-of-plane directions suggest anisotropic superconducting behavior in the R-N_8/S_2 superlattice. Additionally, a BKT transition with a T_{BKT} of 6.80 K was also observed. Above all imply the presence of 2D superconducting feature in the R-N_8/S_2, which is consistent with the infinite-layer nickelates reported previously[37,38,56]. However, the superconducting anisotropy in R-N_8/S_2 is much smaller compared to the significant anisotropy observed in $La_{0.8}Sr_{0.2}NiO_2$[56], which had also been observed in the Nd-based infinite-layer nickelates[35]. The superconducting anisotropy difference between La-based and Nd-based nickelates may due to the influence from rare-earth 4f moments[37,39]. All the experimental results for the superconducting properties of R-N_8/S_2 superlattice are in great agreement with those of $Nd_{0.8}Sr_{0.2}NiO_2$ films. These facts indicate that the $SrTiO_3$ interlayers have no evident enhancement to the superconductivity of the infinite-layer nickelates in this artificial superlattice. It is different from the FeSe/$SrTiO_3$ interface, where the interface effect significantly enhances superconductivity[26]. This suggests that the superconductivity in the superlattice originates from the intrinsic properties of the infinite-layer nickelates, it is also confirmed in recently free-standing infinite-layer nickelates[57,58].

In summary, we had successfully achieved superconductivity with a $T_{c,onset}$ of 12.5 K in the $(Nd_{0.8}Sr_{0.2}NiO_2)_8/(SrTiO_3)_2$(R-$N_8$/$S_2$) superlattice using the two-step method[2]. We observed a structural transition modulated by the thickness of the nickelate layers within the reduced nickelate superlattice. High-resolution HADDF-STEM and iDPC images show that the superlattice R-N_3/S_2 with the thinner nickelate-thickness exhibits partially reduced and disordered phases even after the fully reduction process, whereas the thicker R-N_8/S_2 displays a purely periodic infinite-layer structure. Measurements of anisotropic magnetoresistance and current-voltage characteristic curves indicate a 2D superconducting feature of R-N_8/S_2. Collectively, the findings on the superconducting properties of the infinite-layer nickelate superlattice closely mirror those of $Nd_{0.8}Sr_{0.2}NiO_2$ single films. This suggests that the interface between $SrTiO_3$ and the infinite-layer nickelate has no substantial impact on its superconducting behavior, serving as indirect evidence of the intrinsic superconductivity of infinite-layer nickelates. The realization of superconducting infinite-layer superlattice nickelates opens up possibilities for further interfacial modulation of superconducting films in infinite-layer nickelates and the fabrication of devices. In addition, it also provides a new perspective for understanding the effect of interfaces on the superconductivity of infinite-layer nickelates, which is promising for further studies of the mechanisms of unconventional superconductivity.

Methods

Film growth

The pristine perovskite $[(Nd_{0.8}Sr_{0.2}NiO_3)_n/(SrTiO_3)_m]_{10}$ superlattices were grown on TiO_2-terminated (001) $SrTiO_3$ substrates of size 5 × 5 × 0.5 mm^3 by pulsed laser deposition using a KrF excimer laser (λ = 248 nm). The laser fluence and repetition rate were mixed at 2.5 J/cm^2 and 4 Hz. Oxygen partial pressure and substrate temperature during growth were controlled at 600 °C and 0.1 mbar, respectively. During the growth process, Reflection High-Energy Electron Diffraction (RHEED) was used to in situ monitor the thickness of $Nd_{0.8}Sr_{0.2}NiO_3$ and $SrTiO_3$ layers, respectively. A single crystal $SrTiO_3$ and a $Nd_{0.8}Sr_{0.2}Ni_{1.15}O_3$ polycrystalline target were used during the deposition. The $Nd_{0.8}Sr_{0.2}Ni_{1.15}O_3$ polycrystalline target precursors were prepared by high temperature sintering. Nd_2O_3, $SrCO_3$ and NiO powder were mixed and dispersed with ethanol and ball milling for 24 h. The dried powder was then decarburized at 1200 °C for 12 h, re-ground and mixed, then pressed into a cylindrical target, and sintered at 1350 °C for 12h[2].

Reduction process

The pristine samples were cut into four pieces with a size of 2.5 × 2.5 × 0.5 mm^3. Each piece was put in an alumina crucible with CaH_2 powder (~1 g) without directly contact. Then the crucible was heated to 320 °C and maintained for 10–20 h in a vacuum chamber with a background air pressure of 10^{-5} mbar, with heating and cooling rates of 10 °C/min. In order to ensure that the superlattice samples of different thicknesses are fully reduced, the reduction time was continuously increased. After reduction, the vacuum chamber was restored to atmospheric pressure.

Sample characterization

Surface morphologies were acquired using an atomic force microscope (AFM) in contact mode, and their root-mean-square (RMS) roughness values were analyzed using Gwyddion software. The structural properties of films were characterized by the X-ray diffraction (XRD) patterns and reciprocal space mapping (RSM) using a monochromated Cu-K_α radiation (λ = 0.154 nm). Film thicknesses were measured by X-ray reflectivity (XRR) and fitted by Genx software. The transport behaviors were measured in a van-der-Pauw geometry with Al wire bonded contacts using a Quantum Design Physical Property Measurement System (PPMS-9T). Current-voltage characteristic curves were measured by four-probe method using a source meter unit (Keithley 2400). HAADF-STEM and iDPC-STEM experiments were carried out at an aberration-corrected FEI Titan Themis G2 operated at 300 kV.

X-ray absorption measurements

X-ray absorption spectroscopy (XAS) and X-ray linear dichroism (XLD) were measured at the beamlines MCD-A and MCD-B (Soochow Beamline for Energy Materials) at the Hefei National Synchrotron Radiation Laboratory (NSRL). In the Total Electron Yield (TEY) mode, the Ni $L_{2,3}$-edge was measured along the direction of normal incidence and grazing incidence, the grazing incidence angle is 15°.

Data availability

The data that support the findings of this study are available from the corresponding author upon request. Source data are provided with this paper.

Code availability

The code used in this study (for XRR fit) is available from the corresponding author on request. Or it can be accessed at https://aglavic.github.io/genx/doc/tutorials/simple_reflectivity.html#getting-started.

References

1. Bednorz, J. G. & Müller, K. A. Possible high T_c superconductivity in the Ba–La–Cu–O system. *Z. f.ür. Phys. B Condens. Matter* **64**, 189–193 (1986).
2. Li, D. et al. Superconductivity in an infinite-layer nickelate. *Nature* **572**, 624–627 (2019).
3. Osada, M., Wang, B. Y., Lee, K., Li, D. & Hwang, H. Y. Phase diagram of infinite layer praseodymium nickelate $Pr_{1-x}Sr_xNiO_2$ thin films. *Phys. Rev. Mater.* **4**, 121801 (2020).
4. Osada, M. et al. Nickelate Superconductivity without Rare-Earth Magnetism: (La,Sr)NiO_2. *Adv. Mater.* **33**, 2104083 (2021).
5. Zeng, S. et al. Superconductivity in infinite-layer nickelate $La_{1-x}Ca_xNiO_2$ thin films. *Sci. Adv.* **8**, eabl9927 (2022).
6. Wei, W., Vu, D., Zhang, Z., Walker, F. J. & Ahn, C. H. Superconducting $Nd_{1-x}Eu_xNiO_2$ thin films using in situ synthesis. *Sci. Adv.* **9**, eadh3327 (2023).
7. Pan, G. A. et al. Superconductivity in a quintuple-layer square-planar nickelate. *Nat. Mater.* **21**, 160–164 (2022).
8. Sun, H. L. et al. Signatures of superconductivity near 80 K in a nickelate under high pressure. *Nature* **621**, 493–498 (2023).
9. Zhu, Y. et al. Superconductivity in pressurized trilayer $La_4Ni_3O_{10-\delta}$ single crystals. *Nature* **631**, 531–536 (2024).
10. Zeng, S. et al. Phase Diagram and Superconducting Dome of Infinite-Layer $Nd_{1-x}Sr_xNiO_2$ Thin Films. *Phys. Rev. Lett.* **125**, 147003 (2020).
11. Li, D. et al. Superconducting Dome in $Nd_{1-x}Sr_xNiO_2$ Infinite Layer Films. *Phys. Rev. Lett.* **125**, 027001 (2020).
12. Gu, Q. et al. Single particle tunneling spectrum of superconducting $Nd_{1-x}Sr_xNiO_2$ thin films. *Nat. Commun.* **11**, 6027 (2020).
13. Cheng, B. et al. Evidence for *d*-wave superconductivity of infinite-layer nickelates from low-energy electrodynamics. *Nat. Mater.* **23**, 775–781 (2024).
14. Ding, X. et al. Cuprate-like electronic structures in infinite-layer nickelates with substantial hole dopings. *Natl Sci. Rev.* **11**, nwae194 (2024).
15. Sun, W. et al. Electronic Structure of Superconducting Infinite-Layer Lanthanum Nickelates. Preprint at https://arxiv.org/abs/2403.07344 (2024).
16. Zaanen, J., Sawatzky, G. A. & Allen, J. W. Band gaps and electronic structure of transition-metal compounds. *Phys. Rev. Lett.* **55**, 418–421 (1985).
17. Hepting, M. et al. Electronic structure of the parent compound of superconducting infinite-layer nickelates. *Nat. Mater.* **19**, 381–385 (2020).
18. Keimer, B., Kivelson, S. A., Norman, M. R., Uchida, S. & Zaanen, J. From quantum matter to high-temperature superconductivity in copper oxides. *Nature* **518**, 179–186 (2015).
19. Hayward, M. A., Green, M. A., Rosseinsky, M. J. & Sloan, J. Sodium Hydride as a Powerful Reducing Agent for Topotactic Oxide Deintercalation: Synthesis and Characterization of the Nickel(I) Oxide LaNiO2. *J. Am. Chem. Soc.* **121**, 8843–8854 (1999).
20. Lu, H. et al. Magnetic excitations in infinite-layer nickelates. *Science* **373**, 213–216 (2021).
21. Werner, P. & Hoshino, S. Nickelate superconductors: Multiorbital nature and spin freezing. *Phys. Rev. B* **101**, 041104 (2020).
22. Hu, L. H. & Wu, C. J. Two-band model for magnetism and superconductivity in nickelates. *Phys. Rev. Res.* **1**, 032046 (2019).
23. Zhang, Y.-H. & Vishwanath, A. Type-II t–J model in superconducting nickelate $Nd_{1-x}Sr_xNiO_2$. *Phys. Rev. Res.* **2**, 023112 (2020).
24. Reyren, N. et al. Superconducting Interfaces Between Insulating Oxides. *Science* **317**, 1196–1199 (2007).
25. Gozar, A. et al. High-temperature interface superconductivity between metallic and insulating copper oxides. *Nature* **455**, 782–785 (2008).
26. Wang, Q.-Y. et al. Interface-Induced High-Temperature Superconductivity in Single Unit-Cell FeSe Films on $SrTiO_3$. *Chin. Phys. Lett.* **29**, 037402 (2012).
27. Norton, D. P. et al. Superconductivity in $SrCuO_2$-$BaCuO_2$ Superlattices: Formation of Artificially Layered Superconducting Materials. *Science* **265**, 2074–2077 (1994).
28. Ortiz, R. A. et al. Superlattice approach to doping infinite-layer nickelates. *Phys. Rev. B* **104**, 165137 (2021).
29. Yang, C. et al. Thickness-Dependent Interface Polarity in Infinite-Layer Nickelate Superlattices. *Nano Lett.* **23**, 3291–3297 (2023).
30. Lee, K. et al. Aspects of the synthesis of thin film superconducting infinite-layer nickelates. *APL Mater.* **8**, 041107 (2020).
31. Zeng, S. et al. Origin of a Topotactic Reduction Effect for Superconductivity in Infinite-Layer Nickelates. *Phys. Rev. Lett.* **133**, 066503 (2024).
32. Ding, X. et al. Critical role of hydrogen for superconductivity in nickelates. *Nature* **615**, 50–55 (2023).
33. Goodge, B. H. et al. Resolving the polar interface of infinite-layer nickelate thin films. *Nat. Mater.* **22**, 466–473 (2023).
34. Yang, C. et al. Direct observation of strong surface reconstruction in partially reduced nickelate films. *Nat. Commun.* **15**, 378 (2024).
35. Wang, B. Y. et al. Isotropic Pauli-limited superconductivity in the infinite-layer nickelate $Nd_{0.775}Sr_{0.225}NiO_2$. *Nat. Phys.* **17**, 473–477 (2021).
36. Xiang, Y. et al. Physical Properties Revealed by Transport Measurements for Superconducting $Nd_{0.8}Sr_{0.2}NiO_2$ Thin Films. *Chin. Phys. Lett.* **38**, 047401 (2021).
37. Wang, B. Y. et al. Effects of rare-earth magnetism on the superconducting upper critical field in infinite-layer nickelates. *Sci. Adv.* **9**, eadf6655 (2023).
38. Ji, H. et al. Rotational symmetry breaking in superconducting nickelate $Nd_{0.8}Sr_{0.2}NiO_2$ films. *Nat. Commun.* **14**, 7155 (2023).
39. Chow, L. E. et al. Dimensionality control and rotational symmetry breaking superconductivity in square-planar layered nickelates. Preprint at https://arxiv.org/abs/2301.07606 (2023).
40. Samal, D. et al. Experimental evidence for oxygen sublattice control in polar infinite layer $SrCuO_2$. *Phys. Rev. Lett.* **111**, 096102 (2013).
41. Liao, Z. L. et al. Large orbital polarization in nickelate-cuprate heterostructures by dimensional control of oxygen coordination. *Nat. Commun.* **10**, 589 (2019).
42. Kawai, M. et al. Orientation Change of an Infinite-Layer Structure $LaNiO_2$ Epitaxial Thin Film by Annealing with CaH_2. *Cryst. Growth Des.* **10**, 2044–2046 (2010).
43. Zhong, Z., Koster, G. & Kelly, P. J. Prediction of thickness limits of ideal polar ultrathin films. *Phys. Rev. B* **85**, 121411 (2012).
44. Zeng, S. W. et al. Observation of perfect diamagnetism and interfacial effect on the electronic structures in infinite layer $Nd_{0.8}Sr_{0.2}NiO_2$ superconductors. *Nat. Commun.* **13**, 743 (2022).
45. Song, D. et al. Visualization of Dopant Oxygen Atoms in a $Bi_2Sr_2CaCu_2O_{8+\delta}$ Superconductor. *Adv. Funct. Mater.* **29**, 1903843 (2019).
46. Ikeda, A., Krockenberger, Y., Irie, H., Naito, M. & Yamamoto, H. Direct observation of infinite NiO_2 planes in $LaNiO_2$ films. *Appl. Phys. Express* **9**, 061101 (2016).
47. Hawthorn, D. G. et al. Resonant elastic soft x-ray scattering in oxygen-ordered $YBa_2Cu_3O_{6+\delta}$. *Phys. Rev. B* **84**, 075125 (2011).
48. Zhang, J. et al. Large orbital polarization in a metallic square-planar nickelate. *Nat. Phys.* **13**, 864–869 (2017).
49. Hua, X. et al. Superconducting stripes induced by ferromagnetic proximity in an oxide heterostructure. *Nat. Phys.* **20**, 957–963 (2024).
50. Saito, Y., Kasahara, Y., Ye, J., Iwasa, Y. & Nojima, T. Metallic ground state in an ion-gated two-dimensional superconductor. *Science* **350**, 409–413 (2015).

51. Xing, Y. et al. Ising Superconductivity and Quantum Phase Transition in Macro-Size Monolayer NbSe2. *Nano Lett.* **17**, 6802–6807 (2017).
52. Harper, F. E. & Tinkham, M. The Mixed State in Superconducting Thin Films. *Phys. Rev.* **172**, 441–450 (1968).
53. Zhao, Q. et al. Isotropic Quantum Griffiths Singularity in Nd0.8Sr0.2NiO2 Infinite-Layer Superconducting Thin Films. *Phys. Rev. Lett.* **133**, 36003 (2024).
54. Saito, Y., Nojima, T. & Iwasa, Y. Highly crystalline 2D superconductors. *Nat. Rev. Mater.* **2**, 16094 (2016).
55. Nelson, D. R. & Halperin, B. I. Dislocation-mediated melting in two dimensions. *Phys. Rev. B* **19**, 2457–2484 (1979).
56. Sun, W. et al. Evidence for Anisotropic Superconductivity Beyond Pauli Limit in Infinite-Layer Lanthanum Nickelates. *Adv. Mater.* **35**, 2303400 (2023).
57. Yan, S. et al. Superconductivity in Freestanding Infinite-Layer Nickelate Membranes. *Adv. Mater.* **36**, 2402916 (2024).
58. Lee, Y. et al. Millimeter-scale freestanding superconducting infinite-layer nickelate membranes. Preprint at https://arxiv.org/abs/2402.05104 (2024).

Acknowledgements

This work was supported by the National Key R&D Program of China (Grant No. 2022YFA1403000 (Z.L.)), CAS Project for Young Scientists in Basic Research (Grant No. YSBR-100 (Z.L.)), the Fundamental Research Funds for the Central Universities (Grant No. WK2140000019 (Z.L.)), National Nature Science Foundation of China (Grant No. 52272095 (Z.L.) and 12275272 (K.C.)), and Collaborative Innovation Program of Hefei Science Center, Chinese Academy of Sciences (Grant No. 2022HSC-CIP005 (K.C.)). The authors would like to appreciate Beamlines MCD-A and MCD-B (Soochow Beamline for Energy Materials) at NSRL.

Author contributions

Z.L. conceived the research and designed the experiment. W.X. synthesized, reduced the superlattice thin films. W.X., Z.Y and S.H characterized the structures of pristine and as-reduced thin films. W.X., X.G. and J.L. explored the reduction process. Y.He and Q.Z. performed the STEM experiments. W.X., Z.D., Y.Hong, L.Wang and T.W measured electrical properties. W.X., L.Wei, Z.S., L.L. and K.C. performed measurement and analysis of synchrotron soft X-ray absorption spectroscopy. W.X. and Z.L. wrote this manuscript. Y.G., Q.Z., K.C. and Z.L. extensively discussed the results and were involved in writing of the manuscript. All authors contributed to the analysis of the results.

Competing interests

The authors declare no competing interests.

Additional information

Supplementary information The online version contains supplementary material available at https://doi.org/10.1038/s41467-024-54660-w.

Correspondence and requests for materials should be addressed to Yulin Gan, Kai Chen, Qinghua Zhang or Zhaoliang Liao.

Peer review information *Nature Communications* thanks the anonymous reviewers for their contribution to the peer review of this work. A peer review file is available.